Nano-optical photoresponse mapping of superconducting nanowires with enhanced near infrared absorption

Kleanthis Erotokritou[1] ⓘ, **Robert M Heath**[1], **Gregor G Taylor**[1], **Cheng Tian**[1], **Archan Banerjee**[2], **Alessandro Casaburi**[1] ⓘ, **Chandra M Natarajan**[1], **Shigehito Miki**[3,4], **Hirotaka Terai**[3] and **Robert H Hadfield**[1]

[1] School of Engineering, University of Glasgow, Glasgow, G12 8LT, United Kingdom
[2] School of Physics, University of Bristol, Bristol, BS8 1TL, United Kingdom
[3] Advanced ICT Research Institute, National Institute of Information and Communications Technology, 588-2 Iwaoka, Nishi-ku, Kobe, Hyogo 651-2492, Japan
[4] Graduate School of Engineering Faculty of Engineering, Kobe University, 1-1 Rokkodai-cho, Nada, Kobe 657-0013, Japan

E-mail: k.erotokritou.1@research.gla.ac.uk

CrossMark

Abstract

Superconducting nanowire single-photon detectors (SNSPDs) play an important role in emerging optical quantum technologies. We report on advanced nanometric characterization of a high efficiency near infrared SNSPD design based on a low roughness tantalum pentoxide (Ta_2O_5)/silicon dioxide (SiO_2) distributed Bragg reflector (DBR) cavity structure. We have performed high resolution transmission electron microscopy analysis to verify the smoothness of the DBR. Optical reflectance measurements show excellent correspondence with DBR simulations. We have carried out precision nano-optical photoresponse mapping studies at 940 nm wavelength at $T = 3.5$ K, indicating excellent large area device uniformity (peak efficiency 55% at 100 Hz dark count rate (DCR)) with a full width half maximum timing jitter of 60 ps. With manual fibre coupling with single mode fibre, we achieve a system detection efficiency (SDE) of 57.5% at 940 nm wavelength (100 Hz DCR) at $T = 2.3$ K and a low polarization dependence of 1.20 ± 0.03. For coupling with multimode fibre, we achieve SDE of 90% at 940 nm (200 Hz DCR) at $T = 2.3$ K. These SNSPD devices are promising candidates for use in quantum dot photoluminescence studies and optical quantum technology applications.

(Some figures may appear in colour only in the online journal)

1. Introduction

Since the pioneering work of Gol'tsman *et al* demonstrating single-photon detection in niobium nitride (NbN) superconducting nanowires [1], superconducting nanowire single-photon detectors (SNSPDs) have undergone rapid development [2–4]. SNSPDs are extremely sensitive devices, capable of registering the arrival of individual infrared photons with low noise and excellent timing resolution, outperforming off-the-shelf technologies such as semiconductor single-photon avalanche photodiodes and photomultipliers [5]. Thus, SNSPDs have emerged as an important enabling technology for quantum key distribution (QKD) [6, 7], optical

quantum information processing (QIP) [8, 9] and fundamental tests of quantum mechanics [10]. SNSPDs are typically based on an ultra-thin (<10 nm) superconducting films deposited onto a substrate and afterwards patterned to nanoscale dimension (100 nm) nanowires using electron-beam lithography (EBL) and etching [3]. The nanowires are patterned in a meander geometry to increase the sensitive area of the device that is then aligned to the core of a single mode optical fibre for efficient optical coupling [2, 3]. Cooled below the superconducting transition temperature T_c and current-biased just below the critical current I_c of the nanowire, upon the absorption of a single photon the SNSPD will generate an electrical pulse [11, 12]. The absorption of photons in the nanowires can be enhanced through embedding the SNSPD in an optical cavity [13], photonic waveguide [14] or through nanophotonic structures such as nanoantennas [15]. State-of-the-art SNSPDs can offer high detection efficiency (>90% at 1550 nm wavelength) [16, 17] low intrinsic dark count rates (DCR, mHz) [18], low timing jitter (<18 ps full width at half maximum, FWHM) [19] and short reset times (<5 ns) [20]. Moreover, owing to the small superconducting energy gap of the materials employed [21], SNSPDs can offer a wide spectral range from visible to mid infrared wavelengths [21, 22].

Optical QIP requires efficient generation and detection of single-photons [5]. Single-photon source performance is defined by three characteristic properties: firstly, ability to deliver indistinguishable photons, secondly their purity and thirdly their efficiency [23]. The most promising candidates for near infrared (NIR) single-photon generation are InAs/GaAs quantum dot (QD) single-photon sources. These can achieve extremely high purity (>99.99%) [24] and a photon indistinguishability of up to 97% [25]. These QD single-photon sources most commonly have an emission wavelength in the region of 940 nm and state-of-the-art QD single-photon sources at this wavelength are on the point of becoming commercially available [26, 27]. In the NIR wavelength range, the energy of a single photon is of order 1 eV making detection an extremely challenging task. Off-the-shelf semiconductor photon-counters including single-photon avalanche photodiodes (SPADs) and photomultiplier tubes perform very well in the visible range. However, moving into NIR wavelengths, their performance declines [5]. Particularly close to 940 nm wavelength, there is a gap in performance: the detection efficiency of Si SPADs drops steeply beyond 900 nm, whereas InGaAs SPADs [28, 29] typically operate between 1.1–1.6 μm. Therefore, the development of highly efficient detectors with low DCRs and high timing resolution at 940 nm is essential for exploitation of QD sources in secure communications (QKD) [30] and other QIP systems. Most applications with SNSPDs have been focused on telecommunication bands (1310–1550 nm). Nonetheless, to characterise the performance of a QD single-photon source and exploit these sources in QIP applications, highly efficient SNSPDs operating at 940 nm are required. Initial efforts at QD single-photon source characterisation used early generation SNSPDs without an optical cavity and thus with limited efficiency [31, 32]. Very recently, a SNSPD based on NbN in

an optical cavity with a system detection efficiency (SDE) > 80% at 940 nm [33] has been reported and a broadband design (500–1100 nm) with a peak efficiency of 30% at 800 nm [34] has also been reported. Moreover, a design on non-periodic distributed Bragg reflector (DBR) optimized for (650–900 nm) with a peak efficiency of 82.3% at 808 nm [35] has been demonstrated.

In this study we present comprehensive nanometric characterisation of a NbTiN SNSPD design atop a Ta_2O_5/SiO_2 DBR tuned for maximum optical absorption at 940 nm. We present and analyse high resolution transmission electron microscopy (TEM) of the device structure. We map the single-photon response of the device using a novel low temperature nano-optical setup. At 3.5 K, the SNSPD under test exhibits uniform photoresponse under perpendicular illumination, corresponding to a maximum SDE of 55% at 940 nm wavelength under 100 Hz DCR and a FWHM) timing jitter of 60 ps. With a view to deploying this SNSPD design in QD single-photon emitter studies we manually couple a device with single mode optical fibre achieving an SDE of 57.5% at 940 nm wavelength at T = 2.3 K at 100 Hz DCR. Using multimode optical fibre we achieve SDE of 90.0% at 940 nm wavelength at T =2.3 K at 200 Hz DCR.

2. Materials and methods

The NbTiN thin films that were used for this work were deposited by DC reactive sputtering at room temperature at the National Institute of Information and Communications Technology (NICT), Japan [36]. The film thickness was controlled by the deposition rate and deposition time. The inclusion of Ti into NbN thin films allows for higher current density and sheet resistance in comparison to NbN films. As a result, the signal to noise ratio is significantly improved during device characterisation. Additionally, NbTiN films are more forgiving with regards lattice mismatched substrates in comparison to NbN films [37]. Prior to the 7.5 nm NbTiN thin film deposition, the deposition conditions were optimized for a relatively thick NbTiN film. NbTiN alloy target (80% Nb and 20% Ti) was sputtered onto a silicon substrate at ambient temperature with a total pressure of 2 mTorr and 3.0 A discharge current. 100 nm thick NbTiN test films were grown at various nitrogen flow rates while other parameters were kept unchanged, and the superconducting transition temperature, T_c was measured. As soon as the best conditions were reached for the highest T_c for a bulk NbTiN film, the thickness was decreased to below 10 nm by decreasing the deposition time. A critical temperature T_c = 8 K, defined as the resistance–temperature transition mid-point was measured for the 7.5 nm thick NbTiN on top of a DBR optimised for maximum absorption at 940 nm. The DBR consisted of seven periodic Ta_2O_5/SiO_2 bilayers grown via an ion-beam sputtering method [38] on top of a Si substrate as a one-dimensional cavity with a measured reflectance of the bilayers equal to 98% at 940 nm. The number of the bilayer repeats has been carefully chosen as a trade-off between achieving photon absorption in the film above 98% and whilst minimizing
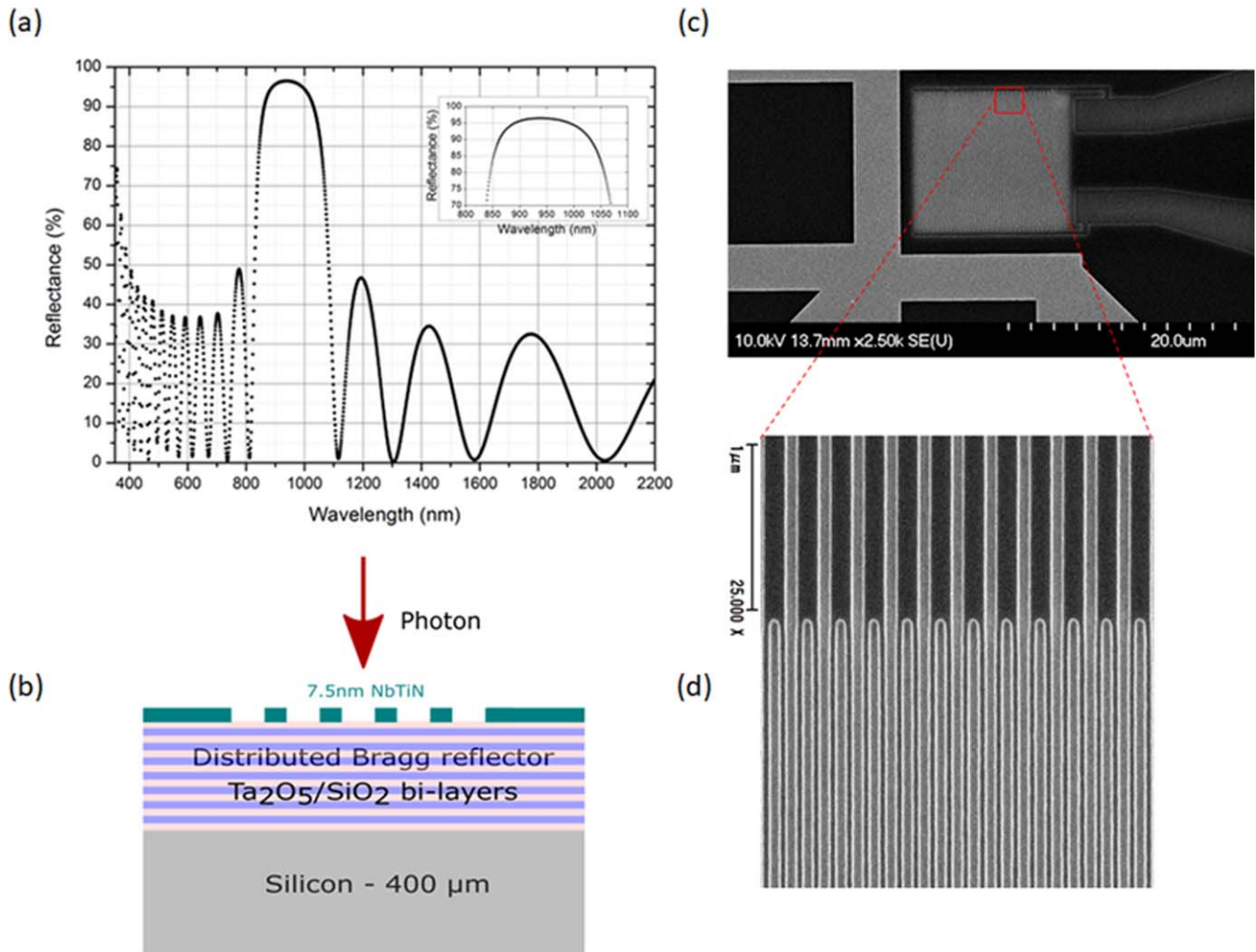
Figure 1. (a) Measured reflectance of DBR consisting of seven repeats of $(Ta_2O_5)/(SiO_2)$ on a Si substrate. (b) Schematic of SNSPD on DBR/Si substrate. (c) Scanning electron micrograph of a NbTiN SNSPD (Device 1) with an active area of $15 \times 15 \ \mu m^2$. (d) Magnified image of an area of the nanowire showing a well-defined linewidth.

mechanical stress/roughness of the top layer where the thin NbTiN film will be grown. This would allow us to maximize the detection efficiency of the device. By taking advantage of this advanced optical structure and using front-side illumination, light absorption in the superconducting NbTiN layer is enhanced. The devices were then patterned and fabricated in the James Watt Nanofabrication Centre at the University of Glasgow. The SNSPD nanowire width was 95 nm and the spacing was 105 nm meandering over a square area of $15 \times 15 \ \mu m^2$ (fill factor 47.5%).

Two EBL steps were used during the fabrication process. EBL was carried out by a Vistec VB6 UHR EHF EBL tool at 100 keV. The first EBL step used a PMMA bilayer positive tone electron-beam resist to pattern alignment markers and bonding contact pads. After development in MIBK: IPA, 100 nm Au (with 3 nm Ti adhesion layer) markers and contact pads were deposited by ultra-high vacuum electron-gun evaporation and lift-off. The nanowire and a $50 \ \Omega$ impedance matched coplanar waveguide electrodes were patterned in the second EBL step with the use of 165 nm ZEP 520 A positive tone electron-beam resist. Then the pattern was transferred

into the NbTiN film by reactive-ion etching with tetrafluromethane (CF_4). The reflectance of the DBR without a NbTiN thin film was measured as a function of wavelength and is illustrated in figure 1(a). The full detector structure from top to bottom was made up from NbTiN/DBR/Si as shown in figure 1(b). A scanning electron micrograph (SEM) of a fabricated NbTiN SNSPD (Device 1) with an active area of 15 x 15 μm^2 is portrayed in figure 1(c) and a magnified SEM image of an area of the nanowire is illustrated in figure 1(d).

The nano-optical characterisation of the NbTiN SNSPD reported in this paper was performed in a cryostat with a base temperature of 3.5 K. Within the cryostat there is a miniature confocal microscope configuration setup [39]. A stack of three piezoelectric stepper motors (Attocube Systems) allow the confocal microscope system to move in *x* and *y*-axes over a large area ($5 \times 5 \ mm^2$). The third piezoelectric motor is used for the focus of the confocal microscope. Additionally, a stack of two independent scanning motors (Attocube Systems) allow for small area 30 μm by 30 μm scanning across the device with sub-nanometre resolution. The three stepper
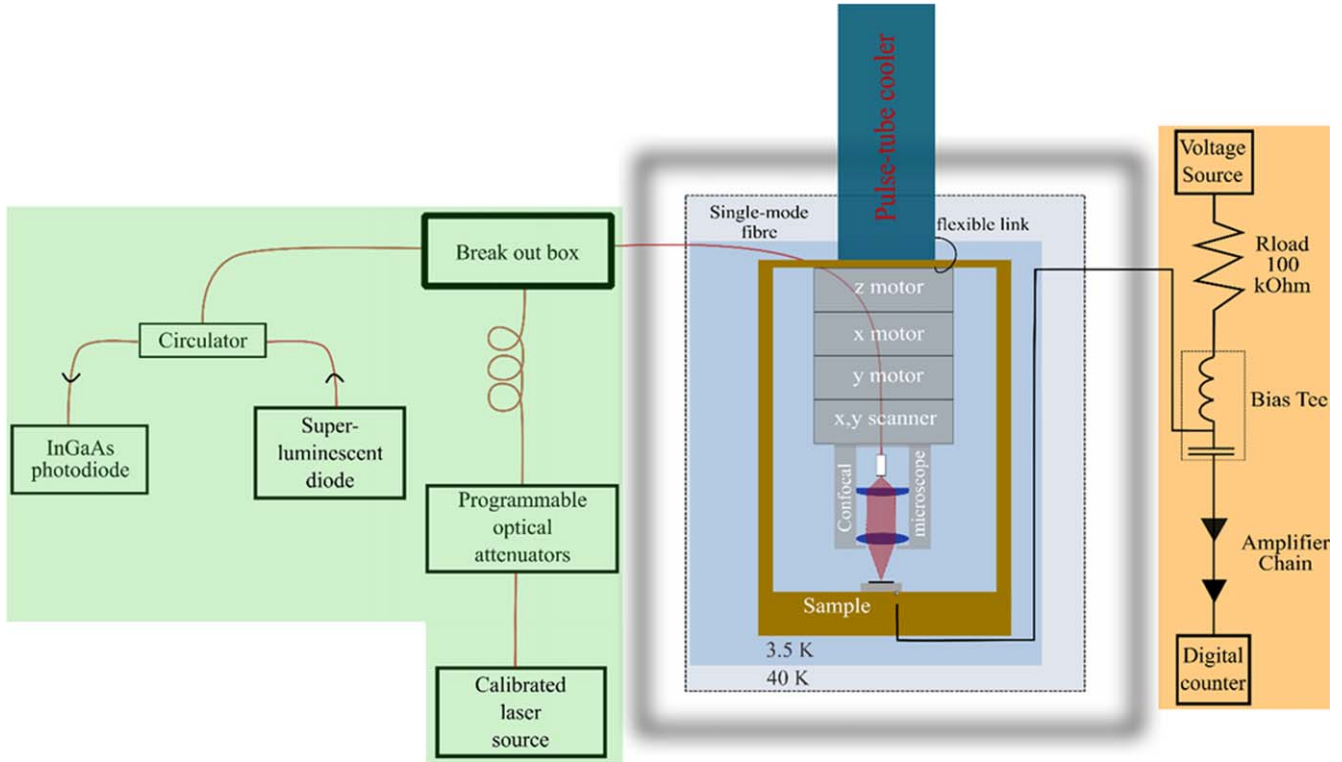
Figure 2. Nano-optical configuration for single-photon measurements on Device 2, as well as room temperature optics and electronics for counts map and detection efficiency measurements. Piezoelectric positioners and confocal microscope are mounted in a gold-plated oxygen-free copper housing, which is attached to a pulse-tube cooler via a flexible thermal link. SMF: single-mode fibre. Green coloured area indicates optical components. Orange coloured area indicates the electronics components. Blue coloured box indicates the low temperature environment.
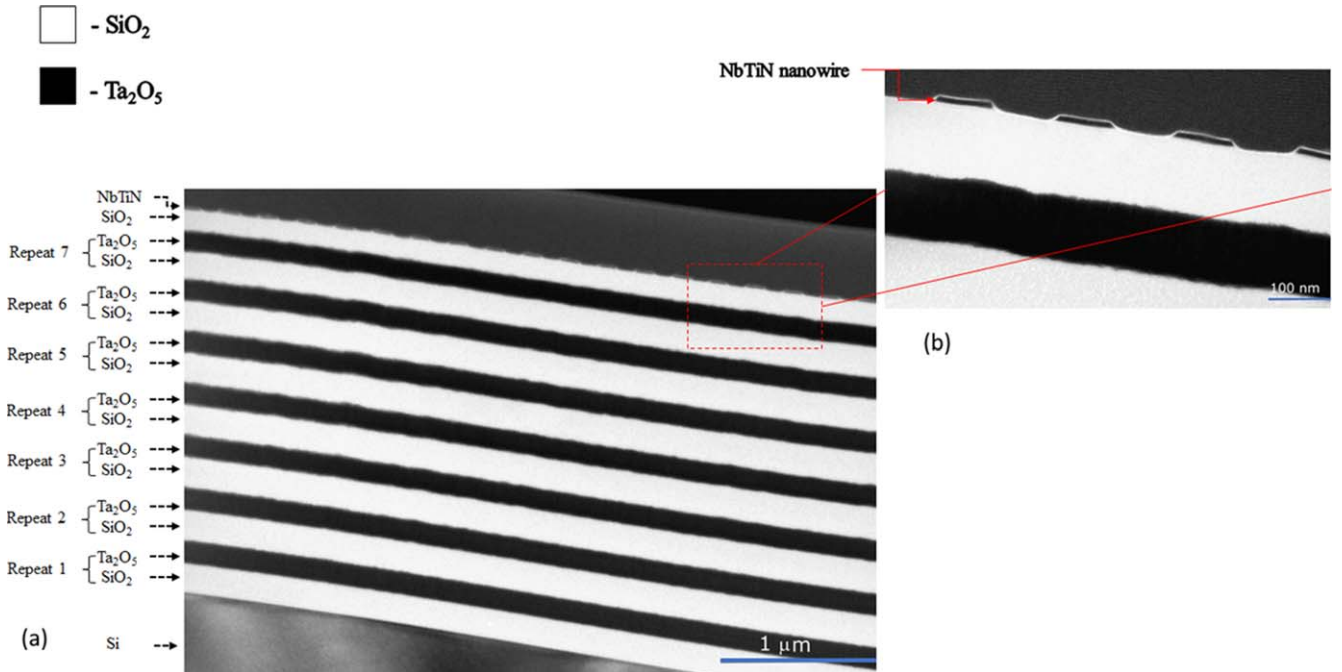

Figure 3. (a) TEM image of the SNSPD cross-section (Device 1) showing the DBR layers atop Si. There are in total seven repeats of SiO_2/Ta_2O_5 with a final SiO_2 layer acting as a $\lambda/4$ cavity before the NbTiN nanowires. (b) Zoomed-in TEM image of the SNSPD cross-section area illustrating the last (repeat 7) of the DBR layers, the $\lambda/4$ cavity SiO_2 layer and the NbTiN nanowires. Note the device is capped with Pt prior to FIB sectioning.

Table 1. Measured thickness of each subsequent bilayer at eight different points across the 5 μm lateral width of the structure of Device 1 imaged in figure 3 and their mean value is presented. Additionally, the rms roughness for each of the SiO$_2$ and Ta$_2$O$_5$ bilayers is presented. SiO$_2$/Ta$_2$O$_5$ bilayer was repeated seven times with a final SiO$_2$ layer acting as a $\lambda/4$ cavity before the NbTiN SNSPD device. The DBR was grown on top of a Si substrate.

Bilayer repeat	SiO$_2$ bilayer thickness (nm)	rms roughness for SiO$_2$ layer (nm)	Ta$_2$O$_5$ bilayer thickness (nm)	rms roughness for Ta$_2$O$_5$ layer (nm)
1	138	1.2	141	0.60
2	185	2.55	150	1.48
3	196	3.21	152	1.79
4	198	4.45	152	1.93
5	202	5.07	152	2.38
6	199	5.89	154	3.44
7	201	6.02	153	4.5
8	191	6.4	—	

motors were controlled by an Attocube ANC150 piezo motion controller whereas, the two scanner motors were controlled by an Attocube ANC200 motion controller. The microscope housing is attached via a flexible thermal link to the second stage of a pulse-tube cooler (Cryomech PT-403). Light attenuated to the single-photon level is delivered to the SNSPD through an optical fibre feedthrough into the cryostat with single-mode fibres (Thorlabs 780HP) and a fibre-based confocal microscope [40] as shown in figure 2.

Measurements of the inductance of the SNSPD devices were carried out with the use of a computer-controlled vector network analyser (VIA Bravo), with frequencies ranging from 0.1 to 50 MHz.

3. Results and discussion

We present results from four devices of the same design from a single wafer fabrication run: device 1 was used for the SEM and TEM studies; device 2 was measured at 3.5 K in our nano-optical mapping setup; devices 3 and 4 were fibre coupled and measured inside a second cryostat with base temperature of 2.3 K.

The structural properties of device 1 have been characterised via high resolution TEM. The TEM facilities available in the School of Physics and Astronomy, University of Glasgow (FEI Tecnai T20 microscope) have been used for this purpose. Before the TEM analysis, electron transparent cross sections have been prepared using a dual beam focussed ion beam system. Figure 3(a) shows a TEM image of the SNSPD cross-section with the DBR substrate. Additionally, in figure 3(b) a zoomed-in TEM image of the SNSPD cross-section active area is shown. During our TEM analysis, we have also examined the thickness variation of each subsequent bilayer at eight different points across the imaged area shown in figure 3 (corresponding to a span of 5 μm) and their mean value was calculated. Additionally, the root-mean-

square (rms) roughness of each subsequent layer was extracted, and it was observed that the rms roughness is increasing from the Si substrate interface up to the top SiO$_2$ layer on which the NbTiN thin film was grown as displayed in table 1. The SiO$_2$ layers show higher roughness in comparison to the Ta$_2$O$_5$ layers (increasing from 1.2 nm for SiO$_2$ and 0.6 nm for Ta$_2$O$_5$ for the first bilayer repeat, to 6.02 nm for SiO$_2$ and 4.50 nm for Ta$_2$O$_5$ in the seventh bilayer repeat). The uppermost SiO$_2$ layer has rms roughness of 6.4 nm over the lateral length scale of 5 μm sampled, which approaches the thickness of the superconducting NbTiN film (7.5 nm) making up the SNSPD device, indicating that the roughness of the DBR may begin to affect the uniformity of the patterned SNSPD device.

Device 2 was mounted and cooled in the setup shown in figure 2. The NbTiN SNSPD device was characterized in terms of basic superconducting properties that include: transition temperature T_c, current–voltage characteristic (I–V curve) and normalized inductance versus normalized bias current (L–I curve). To confirm the uniformity of the nanowires, we analysed the change in inductance while varying the bias current (I_b) [41]. By using this method, is possible to record what happens to the inductance as the SNSPD approaches its I_c. The L–I curve was fitted with the aid of Ginzburg–Landau theoretical model that describes the dependence of the kinetic inductance with respect the bias current (I_b). The inductance was normalized at the value of L_0 that represents the inductance of the SNSPD at $I_b = 0$ and the I_b was normalized at the value of critical current (I_c) that represents the switching current of the SNSPD. Then the data are fitted using equation: $\frac{L_k}{L_{k,0}} = 1 + \frac{4}{9}C^2\left(\frac{I}{I_c}\right)^2$, with inductance L_k at a given $\frac{I}{I_c}$. Basic superconducting properties of NbTiN SNSPD (Device 2) are portrayed in figure 4.

During the fitting of the data, we introduced a parameter $C = I_c/I_c^*$, where I_c^* is derived from the Ginzburg–Landau theoretical prediction and describes the critical current of nanowires with no constrictions. This parameter C was firstly used to explain the effect of a constriction on the cross-sectional area of nanowires with respect their kinetic inductance and their critical current [41]. The obtained value of C for Die 6a was 0.65, whereas the ideal theoretical value for an entirely uniform nanowire without a constriction is $C = 1$. This method could be refined further by the use of BCS theory to obtain a more accurate fit and a precise inductance value [42]; for the purposes of our study the Ginzburg–Landau based model was useful to give an initial indication of nanowire uniformity prior to single-photon response measurements.

To characterise the local detection efficiency of the SNSPD, we used the low temperature confocal miniature microscope to map the surface of the chip and locate the active area of the device. A 1550 nm wavelength superluminescent diode source was used to illuminate the chip. Light reflected from the chip, while the piezoelectric positioners moved, was measured by an InGaAs detector via a circulator at room temperature to create a reflection map. Figure 5(a) illustrates the output voltage signal of the InGaAs
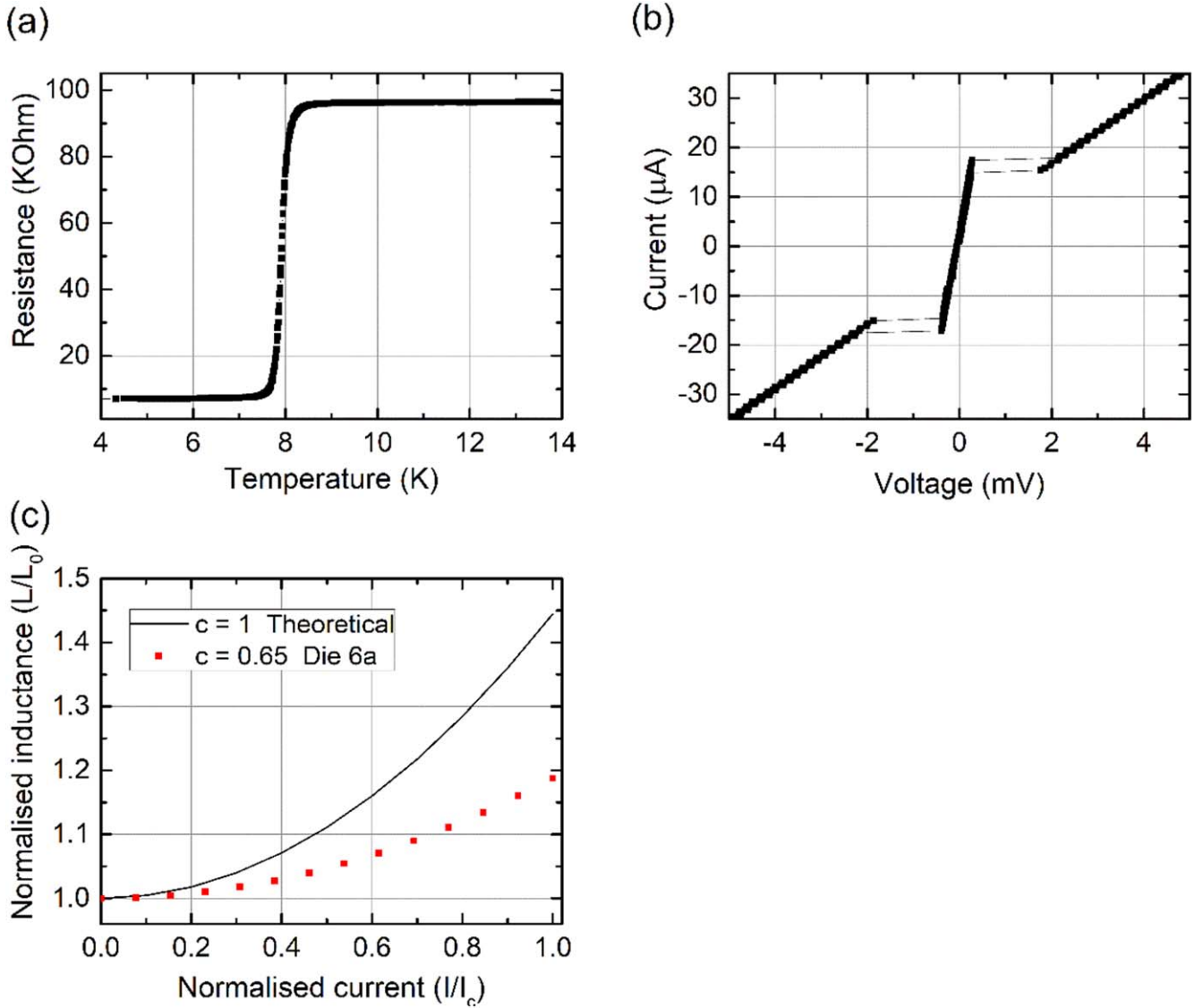
(a)

(b)

(c)

Figure 4. Electrical characterization of Device 2. (a) Device resistance versus temperature, the critical temperature T_c is 8 K defined as the transition mid-point, (b) current–voltage characteristics of same device without a shunting resistor at 3.5 K using a two-wire measurement, the critical current I_c is 18 μA. (c) Normalized inductance for Die 6a versus the variation of the normalized bias current; the inductance was normalized at the value of L_o representing the inductance of the SNSPD at bias current ($I_b = 0$) and the bias current was normalized at the value of I_c of the SNSPD. The black (solid line) represents the theoretical curve for $C = 1$, based on Ginzburg–Landau theory for nanowires with no cross-section constrictions and the red (dotted squares) represent the device Dies 6a with a $C = 0.65$. The data points in all the plots represent the average of repeated measurements and the resulting error bars are comparable or smaller than the data points.

photodiode versus the relative x–y positions indicating the device active area. We then current-biased the device using a bias tee and through room temperature amplification (56 dB) we measured the DCR of the NbTiN SNSPD using an Agilent 53131 universal counter. The photoresponse uniformity of the SNSPD was confirmed by mapping the device area with a 940 nm calibrated pulsed laser at a repetition rate of 1 MHz. The input photon flux illuminating the device was maintained below 1 photon per pulse. The optical spot was scanned across the same area as the photo reflection map figure 5(b). At the highest responding point, the local SDE of the SNSPD was calculated, while the device was biased at 17.0 μA (95% of I_c) indicating a peak SDE of 55% at 100 DCR. By maintaining the spot of the confocal microscope in the same

position used for the SDE measurements, we acquired the timing jitter for that device. A 1550 nm femtosecond fibre laser and an Agilent Infinium DSO80804A 8 GHz oscilloscope were used for the timing jitter measurements illustrated in figure 6. The timing jitter was extracted from the Gaussian fit on the histogram. The FWHM jitter of this device is 60 ps at $I/I_c = 0.85$.

Device 3 from our batch was manually fibre-coupled with a 4.4 μm core diameter 780HP single-mode fibre and cooled on a two-stage type Gifford–McMahon cryocooler (Sumitomo SHI RDK-101D) [43] with a base temperature of $T = 2.3$ K. In figure 7(a) the SDE is illustrated as a function of I_b for this device measured with 940 nm wavelength illumination. Due to the meandering geometry of the nanowire
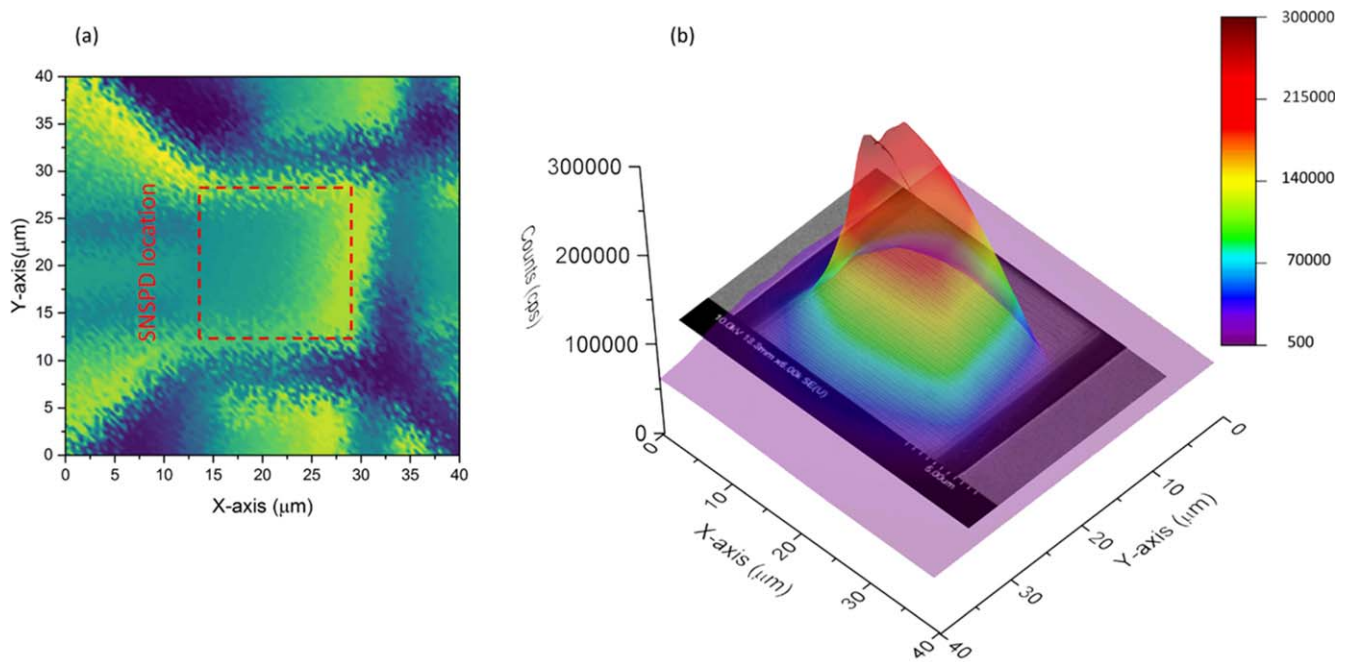
Figure 5. Photoresponse mapping of Device 2 at $T = 3.5$ K. (a) Reflection map of the device active region. (b) Counts map of the device region with $I_b = 15\,\mu$A. The greyscale image on the base of the figure is an SEM image of the active area of the SNSPD.
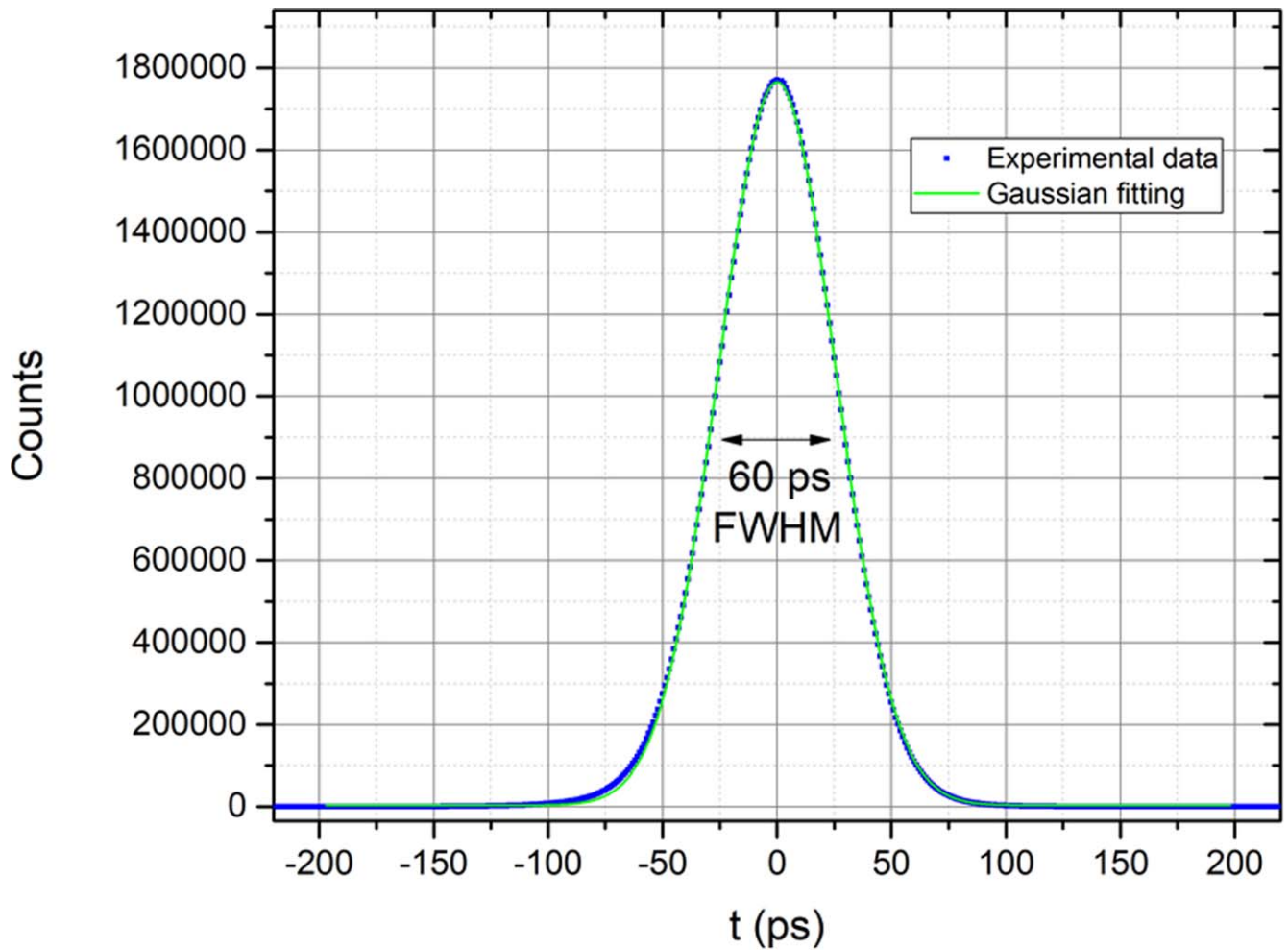

Figure 6. Jitter measurement response histogram (blue data points) with a Gaussian fit (green solid line) at $I_b = 15\,\mu$A. Device 2 measured at $T = 3.5$ K.
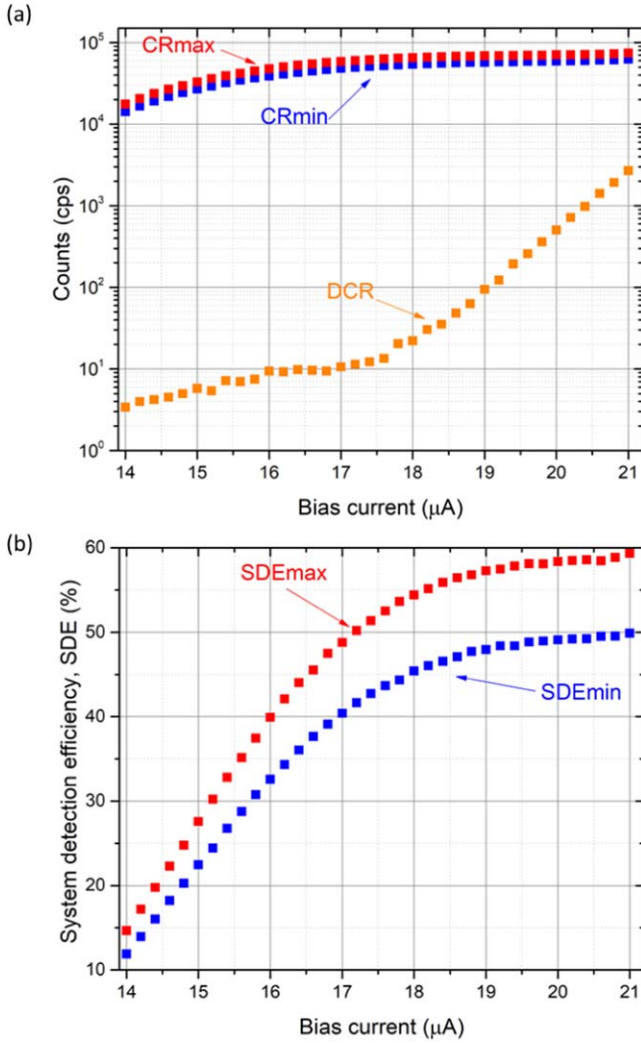
(a)

(b)

Figure 7. Single-mode fibre-coupled measurements of Device 3 at 2.3 K. (a) Dark count rate (DCR) and device count rate in the single-photon regime versus I_{b}. (b) System detection efficiency (SDE) versus bias current, I_{b} for maximum and minimum polarization of the light at $\lambda = 940$ nm and $T = 2.3$ K for device 3. The SDE_{max} (red data points) and SDE_{max} (blue data points) curves were obtained by adjusting the polarization to reach the maximum and minimum count rate of the SNSPD.
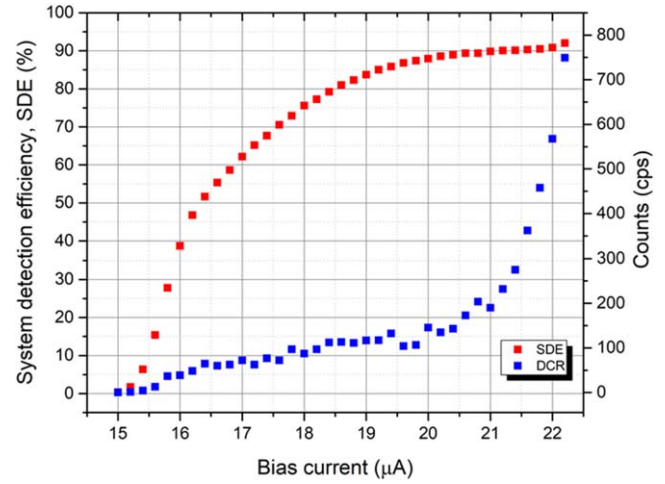

Figure 8. Multimode fibre-coupled measurements of Device 4 at 2.3 K. SDE at 940 nm wavelength (unpolarized illumination) and DCR as a function of bias current.

that multimode fibre coupling further enhances the SDE, reaching 90% for 200 Hz without polarization control.

4. Conclusion

In this study, we have designed and fabricated a new $15 \times 15\ \mu m^2$ SNSPD design atop a DBR cavity comprising seven SiO_2/Ta_2O_5 bilayer repeats optimized for 940 nm wavelength. We have employed advanced nanometric characterization and low temperature measurement techniques to gain insight into the device uniformity and performance. Device 2 from the same fabrication run was electrically and optically characterized at $T = 3.5$ K in a novel nano-optical photoresponse mapping setup. The best SNSPD device showed an overall SDE = 55% at $\lambda = 940$ nm (DCR = 100 Hz) and a timing jitter of 60 ps at $I/I_c = 0.95$. Additionally, devices 3 and 4 from the same fabrication run were manually fibre-coupled and optically characterized at $T = 2.3$ K. Device 3, coupled with single mode fibre (4.4 μm core diameter), showed an overall SDE = 57.5% at $\lambda = 940$ nm (DCR = 100 Hz), and a low polarization dependence of 1.20 ± 0.03. Device 4 coupled with multi-mode fibre (9 μm core diameter) showed a maximum SDE of 90% with unpolarized illumination at 940 nm wavelength. During the manual fibre coupling, it was challenging to minimise the coupling losses and a future direction would be to adopt a self-aligning scheme that will require patterning the devices in a keyhole structure that can fit the ferrule of single-mode fibre and will minimise coupling losses [2, 44]. In our device structure, this requires further technological development, as a deep anisotropic etch process has to be developed not just for the Si wafer, but also for the DBR heterostructure. With self-alignment, we would expect high SDE to be consistently achieved. Also, use of anti-reflection coated fibre [32] would allow a modest increase in SDE. Our TEM analysis shows that the DBR roughness increases with the number of bilayer repeats, and the rms roughness of the top

devices, their efficiency depends on the polarisation of the photons that impinge upon the active area of the device [13]. The polarization of the incident light was controlled with a two-paddle manual fibre-coupled polarizer, that was inserted between the programmable attenuators and the SNSPD, which allowed regulation of the photon-counts from the SNSPD. Figure 7(a) shows the maximum (CRmax) count rate, minimum (CRmin) count rate and DCR of the SNSPD with respect to I_b. Also, we have extracted a maximum (SDEmax) and a minimum (SDEmin) with respect I_b as presented in figure 7(b). A low polarization dependence of 1.20 ± 0.03 was recorded while varying the I_b.

Device 4 from our batch was manually fibre coupled with 9 μm core diameter SMF28 fibre and tested alongside Device 3 at 2.3 K. Figure 8 shows SDE and DCR versus I_b. We see

layer of our DBR stack (6.4 nm) approaches the thickness of the NbTiN superconducting thin film (7.5 nm). Therefore, reducing the number of DBR repeats may achieve the optimal trade-off between optical absorption and SNSPD uniformity. To sum up, high efficiency single-photon detectors are crucial for emerging single-photon quantum technologies using 940 nm wavelength. For example, single-photon purity of emission can be verified by second order correlation functions $g^2(t)$, which indicate the statistical distribution of photons emitted by the source. High efficiency SNSPDs with low dark counts and low timing jitter will improve the acquisition of $g^2(t)$ is improved, yielding lower uncertainty in the measured data for a fixed acquisition time.

Acknowledgments

ORCID iDs

Kleanthis Erotokritou ⬤ https://orcid.org/0000-0002-7284-104X
Alessandro Casaburi ⬤ https://orcid.org/0000-0001-8684-3217

References

[1] Gol'tsman G N, Okunev O, Chulkova G, Lipatov A, Semenov A, Smirnov K, Voronov B, Dzardanov A, Williams C and Sobolewski R 2001 Picosecond superconducting single-photon optical detector *Appl. Phys. Lett.* **79** 705–7

[2] Dauler E A, Grein M E, Kerman A J, Marsili F, Miki S, Nam S W, Shaw M D, Terai H, Verma V B and Yamashita T 2014 Review of superconducting nanowire single-photon detector system design options and demonstrated performance *Opt. Eng.* **53** 081907

[3] Natarajan C M, Tanner M G and Hadfield R H 2012 Superconducting nanowire single-photon detectors: physics and applications *Supercond. Sci. Technol.* **5** 063001

[4] Hadfield R H and Johansson G (ed) 2016 *Superconducting Devices in Quantum Optics* (Berlin: Springer)

[5] Hadfield R H 2009 Single-photon detectors for optical quantum information applications *Nat. Photon.* **3** 696

[6] Sasaki M *et al* 2011 Field test of quantum key distribution in the Tokyo QKD Network *Opt. Express* **19** 10387–409

[7] Sibson P *et al* 2017 Chip-based quantum key distribution *Nat. Commun.* **8** 13984

[8] Silverstone J W *et al* 2014 On-chip quantum interference between silicon photon-pair sources *Nat. Photon.* **8** 104

[9] Schuck C, Guo X, Fan L, Ma X, Poot M and Tang H X 2016 Quantum interference in heterogeneous superconducting-photonic circuits on a silicon chip *Nat. Commun.* **7** 10352

[10] Shalm L K *et al* 2015 Strong loophole-free test of local realism *Phys. Rev. Lett.* **115** 250402

[11] Semenov A D, Gol'tsman G N and Korneev A A 2001 Quantum detection by current carrying superconducting film *Physica* C **351** 349–56

[12] Yang J K, Kerman A J, Dauler E A, Anant V, Rosfjord K M and Berggren K K 2007 Modeling the electrical and thermal response of superconducting nanowire single-photon detectors *IEEE Trans. Appl. Supercond.* **17** 581–5

[13] Rosfjord K M, Yang J K, Dauler E A, Kerman A J, Anant V, Voronov B M, Gol'tsman G N and Berggren K K 2006 Nanowire single-photon detector with an integrated optical cavity and anti-reflection coating *Opt. Express* **14** 527–34

[14] Sprengers J P *et al* 2011 Waveguide superconducting single-photon detectors for integrated quantum photonic circuits *Appl. Phys. Lett.* **99** 181110

[15] Heath R M, Tanner M G, Drysdale T D, Miki S, Giannini V, Maier S A and Hadfield R H 2015 Nanoantenna enhancement for telecom-wavelength superconducting single photon detectors *Nano Lett.* **15** 819–22

[16] Marsili F *et al* 2013 Detecting single infrared photons with 93% system efficiency *Nat. Photon.* **7** 210

[17] Esmaeil Zadeh I, Los J W, Gourgues R B, Steinmetz V, Bulgarini G, Dobrovolskiy S M, Zwiller V and Dorenbos S N 2017 Single-photon detectors combining high efficiency, high detection rates, and ultra-high timing resolution *APL Photonics* **2** 111301

[18] Schuck C, Pernice W H and Tang H X 2013 Waveguide integrated low noise NbTiN nanowire single-photon detectors with milli-Hz dark count rate *Sci. Rep.* **3** 1893

[19] Shcheslavskiy V, Morozov P, Divochiy A, Vakhtomin Y, Smirnov K and Becker W 2016 Ultrafast time measurements by time-correlated single photon counting coupled with superconducting single photon detector *Rev. Sci. Instrum.* **87** 053117

[20] Ivry Y, Surick J J, Barzilay M, Kim C S, Najafi F, Kalfon-Cohen E, Dane A D and Berggren K K 2017 Superconductor–superconductor bilayers for enhancing single-photon detection *Nanotechnology* **28** 435205

[21] Verma V B, Lita A E, Vissers M R, Marsili F, Pappas D P, Mirin R P and Nam S W 2014 Superconducting nanowire single photon detectors fabricated from an amorphous $Mo_{0.75}Ge_{0.25}$ thin film *Appl. Phys. Lett.* **105** 022602

[22] Marsili F, Bellei F, Najafi F, Dane A E, Dauler E A, Molnar R J and Berggren K K 2012 Efficient single photon detection from 500 nm to 5 μm wavelength *Nano Lett.* **12** 4799–804

[23] Shields A J 2007 Semiconductor quantum light sources *Nat. Photon.* **1** 215

[24] Schweickert L *et al* 2018 On-demand generation of background-free single photons from a solid-state source *Appl. Phys. Lett.* **112** 093106

[25] Lodahl P, Mahmoodian S and Stobbe S 2015 Interfacing single photons and single quantum dots with photonic nanostructures *Rev. Mod. Phys.* **87** 347

[26] Sparrow Quantum http://sparrowquantum.com/ (accessed 4 May 2018)

[27] Quandela http://quandela.com/ (accessed 4 May 2018)

[28] Takai I, Matsubara H, Soga M, Ohta M, Ogawa M and Yamashita T 2016 Single-photon avalanche diode with enhanced NIR-sensitivity for automotive LIDAR systems *Sensors* **16** 459

[29] Tosi A, Sanzaro M, Calandri N, Ruggeri A and Acerbi F 2014 Low dark count rate and low timing jitter InGaAs/InP Single-photon avalanche diode *2014 44th European Solid State Device Research Conf. (ESSDERC)* (IEEE) pp 82–5

[30] Waks E, Inoue K, Santori C, Fattal D, Vuckovic J, Solomon G S and Yamamoto Y 2002 Secure communication: quantum cryptography with a photon turnstile *Nature* **420** 762

[31] Hadfield R H, Stevens M J, Mirin R P and Nam S W 2007 Single-photon source characterization with twin infrared-sensitive superconducting single-photon detectors *J. Appl. Phys.* **101** 103104

[32] Zinoni C, Alloing B, Li L H, Marsili F, Fiore A, Lunghi L, Gerardino A, Vakhtomin Y B, Smirnov K V and Gol'tsman G N 2007 Single-photon experiments at telecommunication wavelengths using nanowire superconducting detectors *Appl. Phys. Lett.* **91** 031106

[33] Zhang W J, Li L H, You L X, Huang J, He Y H, Zhang L, Liu X Y, Chen S J, Wang Z and Xie X M 2016 Superconducting nanowire single-photon detector with a system detection efficiency over 80% at 940-nm wavelength *IEEE Photonics J.* **8** 4500908

[34] Vorobyov V V *et al* 2017 Superconducting detector for visible and near-infrared quantum emitters *Opt. Mater. Express* **7** 513–26

[35] Yamashita T, Waki K, Miki S, Kirkwood R A, Hadfield R H and Terai H 2016 Superconducting nanowire single-photon detectors with non-periodic dielectric multilayers *Sci. Rep.* **6** 35240

[36] Wang Z, Miki S and Fujiwara M 2009 Superconducting nanowire single-photon detectors for quantum information and communications *IEEE J. Sel. Top. Quantum Electron.* **15** 1741–7

[37] Yang X, You L, Zhang L, Lv C, Li H, Liu X, Zhou H and Wang Z 2018 Comparison of superconducting nanowire single-photon detectors made of NbTiN and NbN thin films *IEEE Trans. Appl. Supercond.* **28** 1–6

[38] Penn S D *et al* 2003 Mechanical loss in tantala/silica dielectric mirror coatings *Class. Quantum Grav.* **20** 2917

[39] Heath R M, Tanner M G, Casaburi A, Webster M G, San Emeterio Alvarez L, Jiang W, Barber Z H, Warburton R J and Hadfield R H 2014 Nano-optical observation of cascade switching in a parallel superconducting nanowire single photon detector *Appl. Phys. Lett.* **104** 063503

[40] O'Connor J A, Tanner M G, Natarajan C M, Buller G S, Warburton R J, Miki S, Wang Z, Nam S W and Hadfield R H 2011 Spatial dependence of output pulse delay in a niobium nitride nanowire superconducting single-photon detector *Appl. Phys. Lett.* **98** 201116

[41] Kerman A J, Dauler E A, Yang J K, Rosfjord K M, Anant V, Berggren K K, Gol'tsman G N and Voronov B M 2007 Constriction-limited detection efficiency of superconducting nanowire single-photon detectors *Appl. Phys. Lett.* **90** 101110

[42] Annunziata A J, Santavicca D F, Frunzio L, Catelani G, Rooks M J, Frydman A and Prober D E 2010 Tunable superconducting nanoinductors *Nanotechnology* **21** 445202

[43] Miki S, Fujiwara M, Sasaki M and Wang Z 2009 Development of SNSPD system with Gifford–McMahon cryocooler *IEEE Trans. Appl. Supercond.* **19** 332–5

[44] Miller A J, Lita A E, Calkins B, Vayshenker I, Gruber S M and Nam S W 2011 Compact cryogenic self-aligning fiber-to-detector coupling with losses below one percent *Opt. Express* **19** 9102–10